Statistical Modeling of Polarimetric RCS of Road Surfaces for Scattering Simulation and Optimal Antenna Polarization Determination

Wietse Bouwmeester [ID], *Graduate Student Member, IEEE*, Francesco Fioranelli [ID], *Senior Member, IEEE*, and Alexander G. Yarovoy, *Fellow, IEEE*

Abstract—Incoherent backscattering of mm-waves from natural rough surfaces is considered. A novel method is proposed to determine the statistical properties of surface scattering from range profile measurements. The method is based on modeling the road surface as a grid of uncorrelated scattering elements, described by normalized scattering matrices. Using this model, expressions are derived to estimate the mean value and covariance matrix of surface scattering from measurement data. This procedure is then applied to measurement data of four road surface types, namely: 1) dry asphalt, 2) wet asphalt, 3) asphalt covered by basalt gravel, and 4) old asphalt. Using the derived statistical normalized radar cross-section models, two novel applications are proposed. First, a procedure for synthesizing/simulating surface clutter is proposed. This procedure is subsequently used to simulate received power from surfaces comprising patches of one or multiple road surface conditions. Excellent agreement between simulation and measurement results is demonstrated. Second, a method for determining the optimal polarization of the electromagnetic sensing waves used in a single-polarized radar system is proposed. This method is based on factorizing the antenna polarization vector into two bounded parameters, allowing for numerical evaluation of the minima and maxima for targets with a specified scattering matrix. This method is further extended to work with statistical descriptions of scattering matrices by means of Monte Carlo simulations.

Index Terms—Automotive, polarimetry, radar, radar cross section (RCS), simulation, surface clutter.

I. INTRODUCTION

THE amount of vehicles that are equipped with advanced automotive radar systems operating in the 77-GHz band to enhance road safety is rising quickly [1], [2]. These radar systems are mainly used to detect, track, and often to also classify, other road users and obstacles that may be present around the car. Being more compact than their 24-GHz predecessors, modern mm-wave radar systems that operate at 77 GHz receive more intense backscattering from the road surface in front of the vehicle compared to 24-GHz radar systems due to the increased reflectivity of these surfaces at 77 GHz.

Due to the increased backscattering, scattering from road surfaces influences radar measurements more significantly, and therefore, it is important to formulate accurate radar cross-section (RCS) models to properly evaluate the impact of road surface scattering in various automotive radar applications. One of the topics for which polarimetric models of road surfaces are of interest is the recent research in the field of polarimetric automotive radar, a few examples of which can be found in [3], [4], [5], and [6]. In [5] and [6], specifically, the benefits of polarimetric radar for road surface classification are studied. In [5], this is done by computing two features, namely: 1) target entropy and 2) polarimetric pedestal. As these are statistical quantities, accurate statistical polarimetric models of the RCS of road surfaces could be used to validate this method further. In [6], road surface classification on measurement data from polarimetric radar is performed using a convolutional neural network. For this application, a statistical polarimetric model could be used to synthesize lots of surface scattering data on which these networks could be trained.

Statistical RCS models of surface clutter could also be used to increase the accuracy of automotive radar simulation at mm-wave frequencies. For example, in [7] and [8], methods of simulating automotive radar based on ray tracing are proposed but road surface clutter is not considered. In [7], clutter caused by a grass surface is taken into account by placing low polygon count grass chunks randomly on a lawn and applying ray tracing to simulate the response. The synthesis of surface clutter based on statistical RCS models could potentially provide surface clutter returns to simulation results without the need to define complex geometries for surfaces and without the need for ray tracing, potentially decreasing the required computational resources. An approach similar to this is shown to be effective in [9], where scattering matrices from snow slabs are generated based on statistical data previously obtained by the method of moments and finite-element-method-based electromagnetic solvers. Polarimetric statistical RCS models of surfaces could also be of use outside the field of automotive radar and could, for example, be applied to simulate backscattering in synthetic aperture radar. As an example, in [10], the reflectivity is calculated using the small perturbation method and geometrical optics, but realizations of reflectivity could also be generated using statistical RCS models. Also, in ground penetrating radar, normalized RCS

models of surface scattering are needed to provide estimations of surface clutter, as described in [11]. Another general class of applications where normalized RCS models are of use is the determination of optimal polarization of the electromagnetic sensing wave used in radar systems, a few examples of this can be found in [12] and [13].

Even though the applications for normalized RCS models of road surfaces are many, only scarce experimental results on road surface scattering at mm-wave frequencies are presented [14], [15], [16], and research on statistical models of road surface scattering at mm-wave frequencies is relatively limited. In [14], vertically polarized measurements were performed on road surfaces under various conditions. It was found that for vertically polarized waves, wet road surface decreases road surface backscattering while slushy conditions increase it and that snow results in a bimodal distribution for backscattering. In [15], a polarimetric road surface scattering model is developed based on vector radiative transfer theory while statistical properties of road surface scattering, such as correlation of scattering parameters, are not discussed. Similarly, in [17], a theoretical model for road surface scattering under icy conditions is presented but statistical properties of such scattering are not considered. More measurements of radar backscattering at mm-wave frequencies from road surfaces are presented in [16], where it is also found that surface scattering strongly depends on the type of surface while statistical data on road surface scattering are unavailable. Furthermore, some data on road surface measurements are presented in [18] and [19], which also show dependence on road surface conditions at frequencies above and below 77 GHz, respectively, but no statistical analysis is presented.

To address this gap, a novel method to determine the statistical properties of surface scattering from radar measurement data based on the preliminary results in [20] is proposed in this article. The method determines a statistical model of the normalized RCS of a surface-under-test, which is corrected for the influences of the radiation pattern of the measurement antenna and the nonuniform propagation distance from the measurement antenna to different points on the surface. This method is then applied to measurements of real road surfaces under various conditions, and the results of this procedure are presented.

Subsequently, two novel applications of the derived statistical models of normalized RCS of surfaces are introduced in this work. First, a new method is developed to synthesize/simulate road surface scattering based on the extracted models. The results from this simulation can then be used to generate range profiles, range–angle profiles, and range–Doppler spectra for subsequent processing. Excellent agreement between measured range profiles and simulated range profiles is demonstrated. Second, a novel method for determining the optimal sensing wave polarization for single-polarized radar systems is proposed, in order to maximize or minimize backscattering from the road surface. This new method is based on a factorization of the polarization vector and combined with a Monte Carlo approach to use the statistical models found for the measured road surfaces. Alternatively, this approach can also be used to, among others, design polarimetric filters to enhance contrast between various surface types.

The rest of the article is organized as follows: Section II presents the RCS model and the procedure to determine the statistical properties of the normalized RCS of a surface-under-test based on measurement data. Section III describes how to utilize the statistical RCS models to simulate surface scattering and Section IV details a way to find the optimal polarization for minimizing and maximizing returns from surface scattering for single-polarized radar. Section V explains the used measurement setup and procedure to measure road surface conditions while in Section VI, the methods described in the previous sections are applied to the measurement data from real road surfaces. Finally, Section VII concludes this article.

II. NORMALIZED RCS MODELING

To model the normalized RCS of a road surface from measurement data, first the surface is represented as a grid of uncorrelated scattering elements. Each scattering element is characterized by an area A_i, where the subscript i indicates the index of the scattering element, and a normalized scattering matrix with elements $S_{xy,i}^0$, which are samples from a complex multivariate stochastic process. This stochastic process models the normalized scattering parameters associated with a road surface type. Here, the subscripts x and y indicate the polarization basis, which in the case of this work is a horizontal/vertical basis. Therefore, to formulate a model of the normalized RCS of a road surface class, the statistical properties of a stochastic process corresponding to a surface-under-test must be determined from scattering parameter measurements. To do this from measurements made by a radar system, the following two assumptions are made.

1) The surfaces-under-test are isotropic, i.e., the normalized scattering parameters of the surface-under-test do not depend on the azimuth of incident and reflected radiation.
2) Within a range bin, the same angle of incidence is shared by all scattering elements of the surface-under-test.

These assumptions ensure that within a range bin ρ, the equality $S_{xy,i}^0 = S_{xy}^0$ holds. This indicates that all scattering elements within a measured range bin are realizations of the same statistical process.

The mean of the normalized scattering parameters of a surface-under-test can be found in the total measured scattering parameters S_{xy}^{tot} using (1), where the angular brackets denote the mean value of the statistical ensemble of measured scattering parameters

$$\langle S_{xy}^0 (\rho) \rangle = \frac{1}{\sum_{i=1}^{N} \sqrt{R_{xy,i}}} \langle S_{xy}^{\text{tot}} (\rho) \rangle. \tag{1}$$

In this equation, $R_{xy,i}$ indicates the effects of the propagation, antenna gain, scattering element area, and wavelength on the ratio of the received and transmitted power as modeled by the radar equation for the ith scattering element. In $R_{xy,i}$, x and y indicate the polarization basis of the receiving and transmitting antennas, respectively. A derivation of this equation can be found in [20].

As mentioned previously, the surface scattering elements are modeled as independent of and uncorrelated with each other.

However, the two copolarized and the two cross-polarized scattering parameters corresponding to a single scattering element can be correlated with each other, and thus, the covariance of these scattering parameters must also be determined. To determine the covariance of the normalized scattering parameters of a road surface from its measured scattering parameters, the following equation can be used:

$$\text{Cov}\left(S_{xy}^0\left(\rho\right), S_{uv}^0\left(\rho\right)\right) = \frac{\text{Cov}\left(S_{xy}^{\text{tot}}\left(\rho\right), S_{uv}^{\text{tot}}\left(\rho\right)\right)}{\sum_{i=1}^N \sqrt{R_{uv,i}}\sqrt{R_{xy,i}}}. \quad (2)$$

In (2), to express all possible covariance permutations of polarizations, the subscripts u and v are also indicators of the same polarization basis as x and y. Thus, in the case of a horizontal/vertical polarization basis, x, y, u, and v can be H or V. A derivation of this equation can also be found in [20].

The last step in formulating a normalized RCS model of a surface is to determine the probability distribution of the real and imaginary parts of the normalized scattering parameters. The shape of this distribution can be determined from histograms of the measured scattering parameters. When many surface scattering elements are contained within one range bin, as usually is the case with surface scattering from road surfaces at mm-wave frequencies, the measured distributions tend to approach normal distributions. This is explained by the summing of scattering contributions from each scattering element within a range bin, thus leading to a normal distribution due to the central limit theorem. Therefore, the real and imaginary parts of the normalized scattering parameters of a surface scattering element can be modeled as a multivariate normal distribution with mean values and covariance as found from (1) and (2).

However, it should be noted that the procedure presented in this section for finding mean and covariance values does not exclusively work for normally distributed normalized scattering parameters. Namely, only mathematical properties of the mean and covariance are used, and no specific assumptions on the distribution of scattering parameters are made in the derivation of (1) and (2). Thus, these equations can be used to determine the mean and covariance of any arbitrary distribution of S_{xy}^0.

III. SURFACE CLUTTER SYNTHESIS

Once models of the normalized scattering parameters of surfaces are known, they can be used to synthesize/simulate range profiles, range–angle profiles, and range–Doppler spectra of surface clutter. Similar to the previous section, the proposed synthesis method models the surface as many individual scattering elements and computes the contribution of each individual scattering element toward the signal as measured by a radar. The synthesis method comprises the following steps.

1) Model the surface as a collection of discrete surface scattering elements by generating a grid of these elements.
2) Find the incident angles, range, and observation angles for each surface scattering element.
3) For each scattering element, take a sample from a multivariate distribution with mean and covariance corresponding to the angle of incidence for said surface scattering element.

4) Calculate the received electric field strength from each scattering element.
5) Sum the received electric field strength from each scattering element to its corresponding bin.

In step 2, the range to each surface scattering element can be computed by taking the norm of the vector pointing from the antenna to said scattering element. The incident and observation angles can in turn be computed using the equations presented in [21]. Subsequently, the contribution of each scattering element can be found using

$$E_x^{rx} = \sqrt{R_{xy}} S_{xy}^0 E_y^{tx} \quad (3)$$

where R_{xy} is a function of the previously computed range to and observation angles of the surface scattering element. An example of the output of this synthesis process for the copolarized channels is displayed in Fig. 4.

Subsequently, this output can be further processed to compute range profiles, range–angle plots, and range–Doppler spectra. This can be done by specifying the limits and resolution of the to-be-simulated profiles and summing the contribution of each scattering element to its corresponding range, angle, and/or Doppler bin. To compute the azimuth angle of a scattering element in the case of 3-D radar (i.e., a radar that provides range, azimuth, and Doppler information), or both azimuth and elevation angles in the case of 4-D radar (i.e., a radar that also provides elevation information), the theory in [21] can be used. To compute the Doppler or velocity bin, the radial velocity v_r of each scattering element with coordinates x and y can be found as

$$v_r = \frac{v}{\sqrt{x^2 + y^2 + h_r^2}} \quad (4)$$

where h_r is the antenna mounting height and v is the platform velocity, which is assumed to be along the y-axis.

Finally, to create range and range–angle profiles and range–Doppler spectra, the contributions of the scattering elements to the electric field can be summed in the correct bins via

$$F = \sum_{k=1}^M E_{xy,k}^{rx}. \quad (5)$$

Here, F is the desired output representation (e.g., range–Doppler spectrum) and k represents the index of a scattering element for the M surface scattering elements that lie within a certain range, angle, and/or Doppler bin. Thus, F can be a function of range, angle, and Doppler, or all of them or even other bin quantities by which F could be binned. In $E_{xy,k}^{rx}$, the subscripts x and y indicate the receive and transmit polarization, respectively. Note that when $E_{xy,k}^{rx}$ are zero-mean random variables, performing this summing operation will not cause the received field from a range bin to converge to zero when the number of scattering elements within such a range bin increases. This is because the area term in $R_{xy,i}$ is inversely proportional to the number of scattering elements within one range-bin, which results in $E_{xy,k}^{rx}$ decreasing with the square root of the number of scattering elements, as can be seen from (5). This, in turn, leads to the variance of the electric field received in a range bin remaining the same as the variance of a sum of identical independent

distributed random variables is proportional to the number of variables in that sum while the variance of a random variable premultiplied by a constant is the same as the variance of the same random variable postmultiplied by that constant squared. An example output of range profile and range–Doppler spectra can be seen in Figs. 5 and 6, respectively.

IV. OPTIMAL SENSING WAVE POLARIZATION FOR SINGLE-POLARIZED AUTOMOTIVE RADAR

Besides surface clutter synthesis, the polarimetric normalized RCS models can also be used to find the optimal polarization to maximize or minimize the power that is received from a target corresponding to that model by a radar system that uses a single polarization. Furthermore, this analysis could also be used to, for example, design a filter that maximizes the contrast between multiple classes of targets, e.g., a puddle of water on asphalt versus dry asphalt.

Using the polarization vector of an antenna, indicated by $\vec{p}$, which, in a single-polarized radar system, is the same for the transmit and receive antennas, the received power P^{rx} from a target with scattering matrix S can be computed using (6), in which ^{H} indicates the conjugate transpose operator. The polarization vector is the vector that describes the polarization state of a transmitted electromagnetic wave by an antenna and the gain of that same antenna for incoming electromagnetic waves of a certain polarization [22]. Using the polarization vector and the scattering matrix, the received power from a target can be calculated as [23]

$$P^{rx} = \left| \vec{p}^H S \vec{p} \right|. \tag{6}$$

As can be seen from this equation, the received power can be either minimized or maximized by selecting a certain $\vec{p}$.

The polarization vector $\vec{p}$ is defined as follows:

$$\vec{p} = \begin{bmatrix} c_x e^{j\delta_x} \\ c_y e^{j\delta_y} \end{bmatrix}. \tag{7}$$

Here, c_x and c_y describe the gain for the x and y polarized components while δ_x and δ_y describe the phases of those components. As in this problem, the goal is to find the optimum polarization for a single-polarized radar system instead of just maximizing the antenna gain or simply setting it to zero to achieve zero received power, the polarization vector is constrained to have a norm of 1, i.e., $\hat{p}^H \hat{p} = 1$. Polarization vectors that have this property are denoted by $\hat{p}$.

Subsequently, since $\hat{p}^H \hat{p} = 1$, $\hat{p}$ can be factorized as follows:

$$\hat{p} = \begin{bmatrix} A e^{j\delta_x} \\ \sqrt{1-A^2}\, e^{j\delta_y} \end{bmatrix} = e^{j\delta_x} \begin{bmatrix} A \\ \sqrt{1-A^2}\, e^{j(\delta_y - \delta_x)} \end{bmatrix}$$
$$= e^{j\delta_x} \begin{bmatrix} A \\ \sqrt{1-A^2}\, e^{j\delta} \end{bmatrix}. \tag{8}$$

The absolute phase component in the polarization vector $e^{j\delta_x}$ can be neglected as it does not influence the received power as it results in an extra $\left| e^{j\delta_x} \right|$ term in (6) which is always equal to 1. Thus, it can be seen from (8) that $\hat{p}$ can be factorized by two parameters, namely A and δ. Furthermore, A is bounded

between 0 and 1 since $\hat{p}^H \hat{p} = 1$ and δ is bounded between $-180°$ and $+180°$ due to the cyclic nature of the phase. Therefore, the minima and maxima of P^{rx} for a discrete target with a well-known scattering matrix can be determined by numerically computing (6) for an array of values of A and δ bounded by 0 and 1 and $-180°$ and $+180°$, respectively.

Furthermore, in the case of a statistical description of S, the minima and maxima of P^{rx} can be found by means of a Monte Carlo procedure. Namely, a large amount of scattering matrices can be generated using the procedure outlined in Section III. Thereafter, for each scattering matrix, P^{rx} can be calculated as a function of A and δ. Finally, the mean of P^{rx} over the different realizations of S can be taken, from which the maxima and minima can be determined. An example of such a computation is shown in Fig. 12.

V. MEASUREMENTS

The measurement setup is comprised of a vector network analyzer (VNA) connected to a dual-polarized horn antenna to perform polarimetric measurements. The antenna assembly was subsequently placed on a supporting structure that allowed for controlling the angle in the vertical plane of the antenna relative to the surface. This antenna orientation angle is defined as the angle between the surface normal and the antenna broadside. The VNA was set to sweep a frequency range from 75 to 85 GHz in 1001 frequency steps. More details on the measurement setup and its settings can be found in [24].

Measurements were performed to obtain data for three different road surface conditions, as well as two different types of asphalt. The two considered types of asphalt were relatively new asphalt and old asphalt that was scheduled to be replaced shortly after the measurements. As there exist many different types of asphalt, to keep the study presented in this work as comprehensive as practically possible, these two opposing ends of the range of possible asphalt types were selected to investigate the variation of backscattering from asphalt. The considered road surface conditions were the new asphalt type when dry, wet, and covered with basalt gravel as may be encountered during road surface construction or maintenance. In this case, the gravel comprised of basalt rocks ranging in size between 2 and 8 mm. Pictures of the road surface classes are shown in Fig. 1. These four road surface conditions were each measured with antenna orientation angles of 60°, to achieve maximum SNR at short range, and at 90°, to simulate forward-looking radar.

To find a statistical normalized RCS model of the surfaces-under-test, it is important to obtain measurements of surface areas that are uncorrelated with each other. This can be done by ensuring that the antenna beam footprint illuminates a part of the asphalt surface that is at least a few correlation lengths away. Previous investigation has shown that the correlation length of an asphalt road surface is around 2 mm [21]. Therefore, this condition can be achieved by moving the measurement setup a few centimeters between measurements.

To gather sufficient data to compute proper statistics, after calibrating the measurement setup, 50 independent measurements of each surface class were obtained. Subsequently, the measurements were postprocessed to find the total scattering
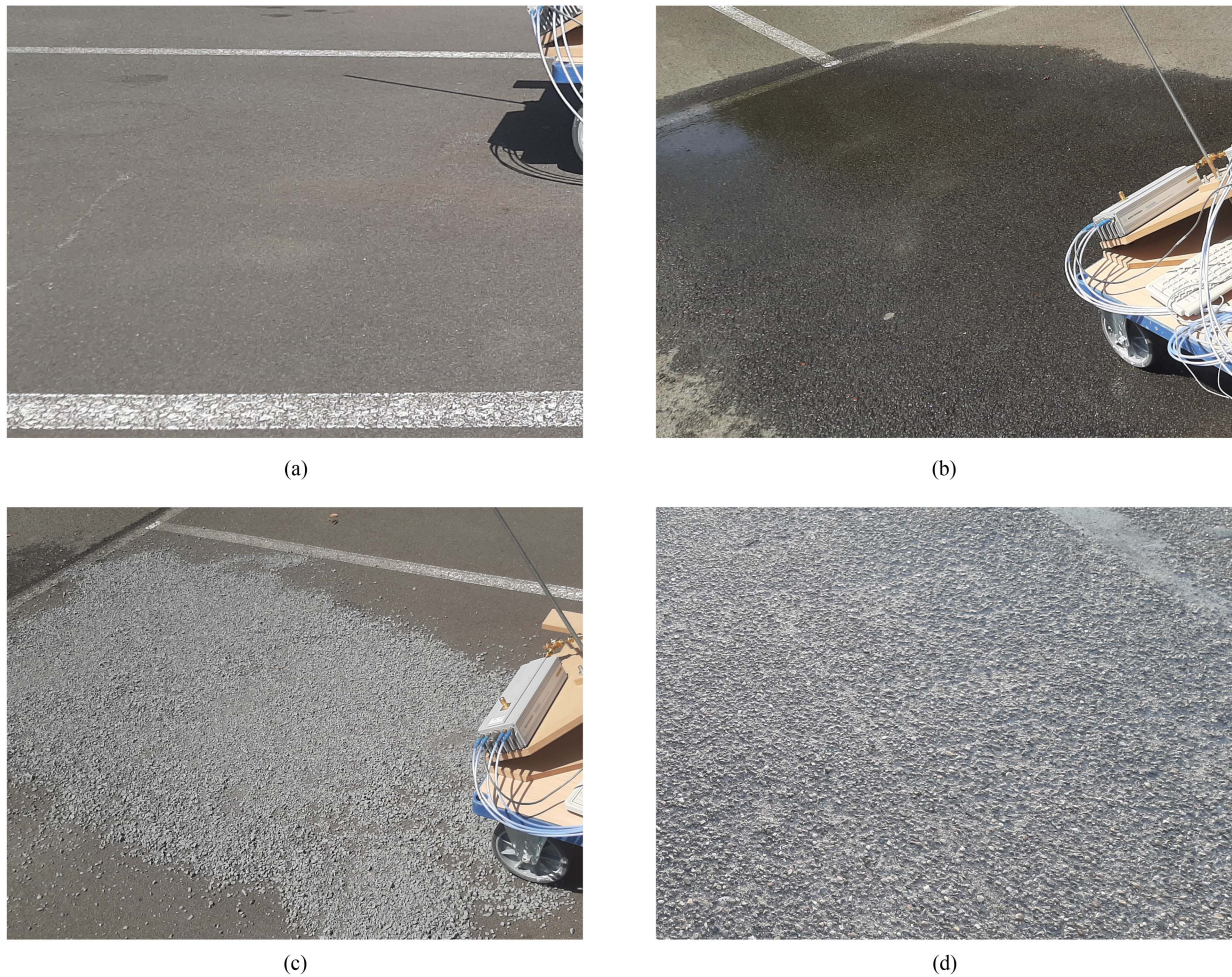
Fig. 1.　Photographs of the three road surface conditions that were measured. (a) Dry asphalt. (b) Wet asphalt. (c) Asphalt covered with basalt gravel with pebble sizes between 2 and 8 mm. In addition, a different patch of old asphalt was also measured (d).

parameters. More details on the calibration of the measurement setup, measurement procedure, and postprocessing can be found in [20] and [24].

VI. Experimental Results and Discussion

In this section, normalized RCS models of the four different road surface classes are determined by applying the procedure described in Section II on the dataset of VNA measurements collected as shown in Section V. The models of the four surfaces are presented in VI-A while the application of these models to simulation of road surface scattering and determination of optimal polarization for single-polarized radar systems are presented in Sections VI-B and VI-C.

A. Normalized RCS of Various Road Surface Conditions

The extracted normalized RCS models of the four measured road surface conditions are shown in Fig. 2(a)–(d). These, re-spectively, show the extracted normalized RCS models of dry asphalt, asphalt covered with water, asphalt covered with basalt split with sizes ranging from 2 to 8 mm, and old asphalt.

Fig. 2(a) shows that for dry asphalt, the two copolar nor-malized RCSs start to differ more and more as the angle of incidence increases. At an incident angle of 40°, the horizontal and vertical normalized RCS are close to -16 dB for both copolar channels, whereas, at 75°, the VV-polarized normalized RCS has decreased to -22 dB and the HH-polarized RCS to -26 dB. This scattering behavior agrees well with known results of backscattering from natural surfaces [25]. Furthermore, it can be seen that both cross-polar normalized RCSs are of the same level due to the monostatic measurement configuration. Also, the cross-polar RCSs are significantly smaller than the copolar ones, which indicates that a limited amount of multiple scat-tering events are occurring at the asphalt surface and within the asphalt medium, or that internal multiple scattering is attenuated strongly by the conductivity of the material.

The wet asphalt shows a smaller RCS for both co- and cross-polarized channels compared to dry asphalt [see Fig. 2(b)]. This is likely due to water—whose permittivity is close to that of asphalt at 77 GHz—filling the cracks and holes in asphalt, increasing the effective flatness of the surface. This is further magnified by the relatively large imaginary part of the complex dielectric constant due to the relatively high conductivity of
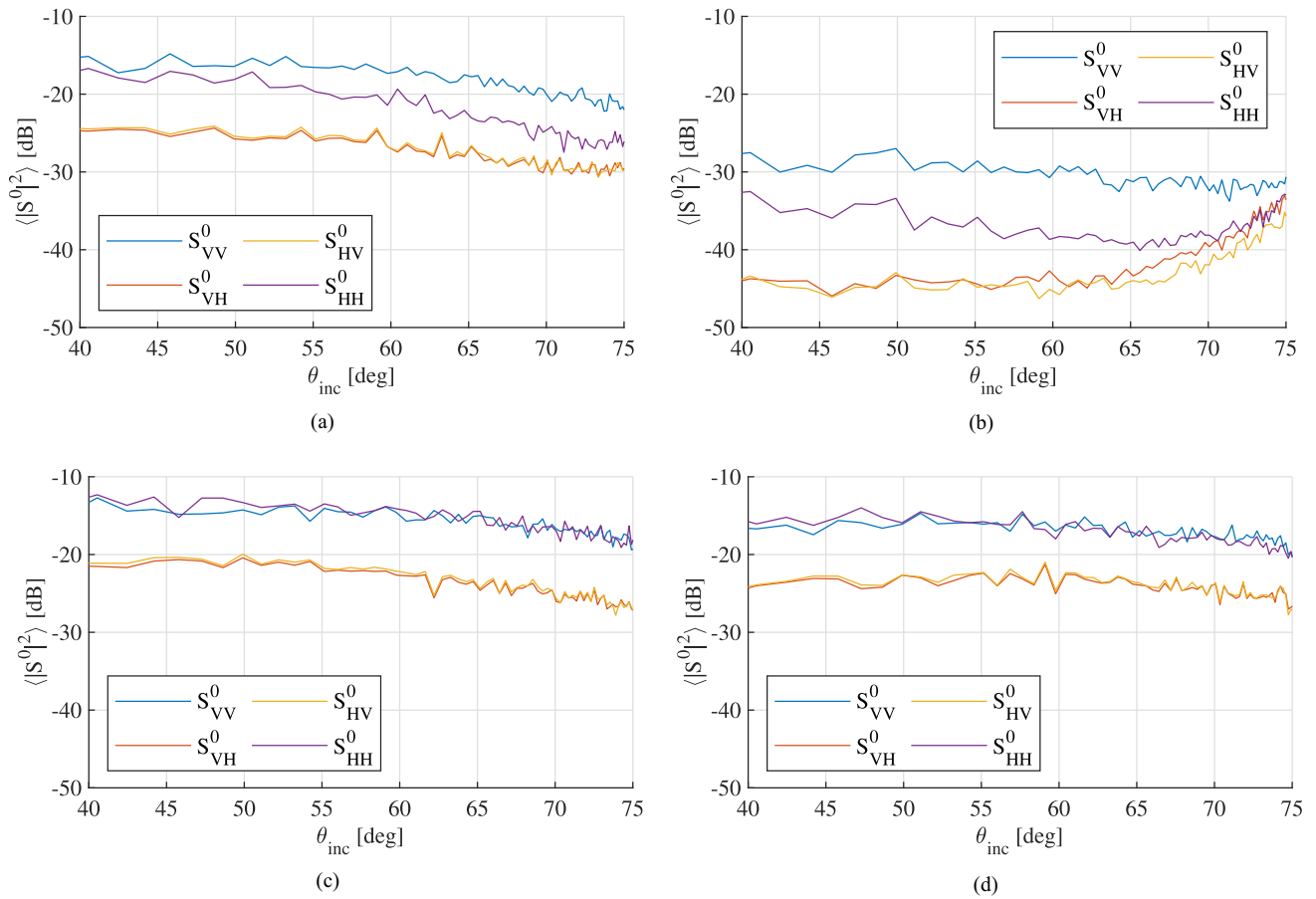
Fig. 2. Normalized RCSs of multiple different road surfaces and conditions. (a) Dry asphalt. (b) Wet asphalt. (c) Asphalt covered by basalt split ranging in size from 2 to 8 mm. (d) Old asphalt.
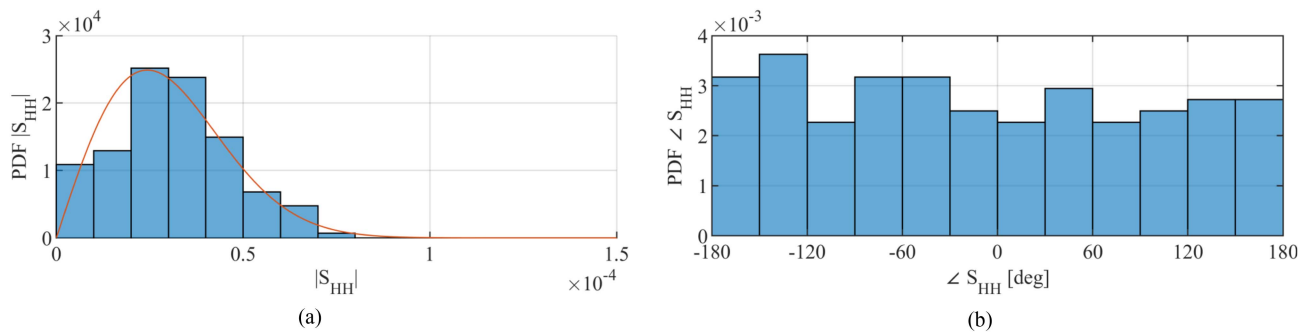

Fig. 3. Histograms of S_{HH} of dry asphalt in the incident angle interval of 59°–61°, normalized to represent the probability density functions. (a) Magnitude, with a comparison to a Rayleigh distribution (in red) with identical variance as the measurement data. (b) Phase.

water. This results in higher reflection coefficients for both polarizations compared to dry asphalt, thus reducing the amount of power scattered back to the radar. It can also be seen that for the wet asphalt, the difference between the HH- and VV-polarized channels is larger than for dry and basalt-covered asphalt. This can also likely be contributed to the water layer increasing the effective surface flatness, whereas the rougher surfaces of the dry and basalt-covered asphalt depolarize the backscattered waves more significantly. Also, it can be seen that the cross-polar normalized RCSs are similar to each other, as expected for reciprocal media when measured in a monostatic configuration.

Furthermore, it can also be observed that the copolar normalized RCSs are significantly smaller than the copolar RCSs, again indicating that the contribution from multiple scattering events is limited.

Note that for the measurements of wet asphalt, the normalized RCSs of the cross-polar channels and the HH-polarized channel start to increase from about 65° and 70°, respectively. This is likely the result of the noise floor of the VNA, which is located around −110 dB when transformed to the time/range-domain. From the 65°/70° point onward, the return from the wet asphalt surface in these three channels is lower than the noise floor, and
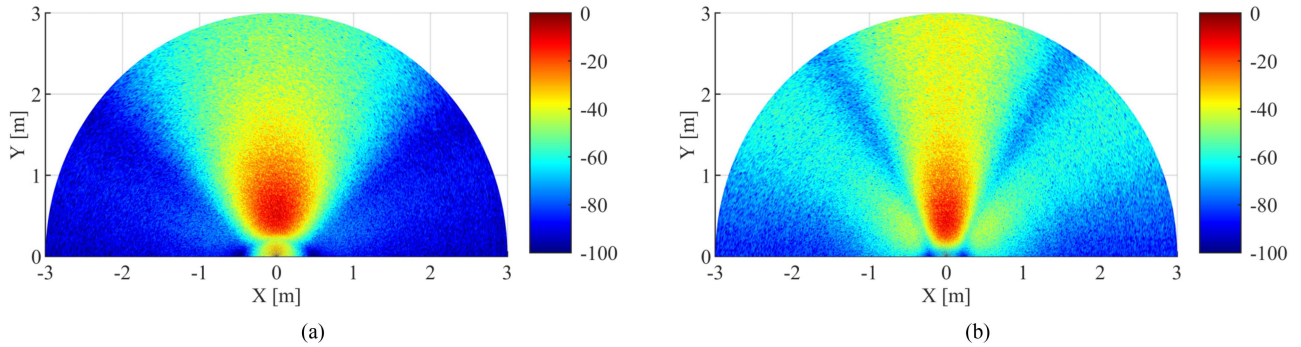
Fig. 4. Normalized received power from surface scattering elements simulating dry asphalt, including effects of propagation losses, scattering element surface area, and the gain of a dual-polarized antenna at a height of 38 cm with an orientation angle of 60°. (a) VV-polarized channel. (b) HH-polarized channel.

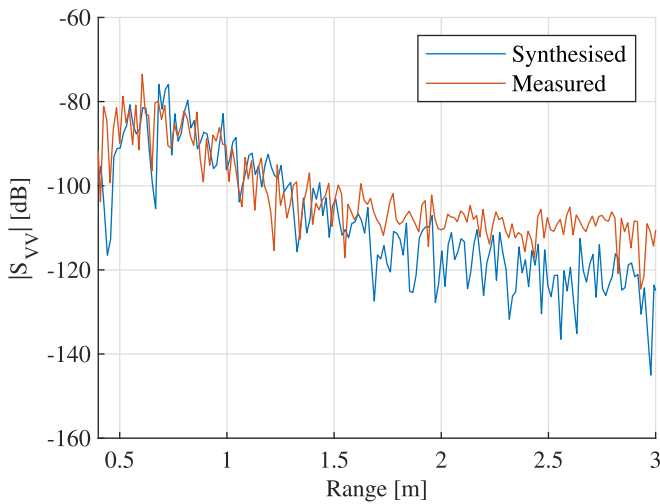Fig. 5. Synthesized range profile of the VV-polarized channel from a uniform dry asphalt road surface compared to measurement data performed on a dry asphalt road surface with a dual-polarized horn antenna with an antenna orientation angle of 60°.

thus, the measured S-parameters are dominated by noise power from the range corresponding to these incident angles onward. As the noise floor is constant, the measured S-parameters for all of the surface beyond these ranges are around -110 dB, independent of the actual range to the surface at those distances. Since the measured S-parameters are divided by the antenna footprint to compensate for differences in antenna gain and propagation losses as shown in (2), the normalized RCS shows an increasing trend for the surface area that is dominated by the constant noise floor. Thus, it can also be concluded that the lower limit of the measurable normalized RCS of a surface with this measurement setup as a function of range can be found by compensating the noise floor value of the VNA for the antenna footprint using (2). As the normalized RCS of the wet surface for the cross-polar and HH-polarized channels is below this lower limit, an apparent increasing normalized RCS with incident angle results, due to the dominant contribution of noise at these ranges.

Furthermore, it can be seen in Fig. 2(c) that the normalized co-polarized RCSs of the basalt-covered asphalt are independent of polarization. In this figure, the copolarized RCSs follow the

shape of a cosine closely, which is indicative of scattering by an electromagnetically rough surface with Lambertian behavior. Also here, the cross-polar normalized RCSs are about 10 dB below the copolar normalized RCSs, again indicating limited contribution from multiple scattering, and these are of about equal magnitude.

Finally, it can be seen that the old asphalt surface type exhibits a scattering behavior in between that of dry new asphalt and new asphalt covered by basalt gravel. It can be seen in Fig. 2(d) that the copolar normalized RCSs are of similar magnitude compared to each other, thus indicating relatively strong depolarization as also occurs for basalt-covered asphalt. However, it can also be seen that the magnitudes of the copolar normalized RCSs of the old asphalt type are lower compared to those of basalt-covered asphalt. This is consistent with the geometrical roughness of the road surfaces, as the measured old asphalt is rougher than the new asphalt type while being smoother than the basalt-covered asphalt. This leads to the observation that the normalized RCSs of road surfaces are more strongly dependent on surface roughness characteristics rather than on their dielectric properties. Also, as with the other road surface classes, it can be seen that the cross-polar normalized RCSs are significantly lower, also indicating that multiple scattering contributions play a limited role for old asphalt.

B. Range Profile and Range–Doppler Synthesis

As described in Section III, the extracted normalized RCS models can be used to synthesize surface scattering in automotive radar scenarios and simulate range profiles and range–Doppler spectra. The first step in such syntheses is to determine a suitable probability distribution that fits the measurement data well. Histograms of the measured magnitude and phase in the 59°–61° incident angle interval of S_{HH} for dry asphalt are shown and compared to a Rayleigh distribution in Fig. 3(a) and (b). It can be seen that a Rayleigh distribution provides a reasonable fit for the magnitude and that the phase seems to approach a uniform distribution. This observation also holds for the other scattering parameters and also applies to those of wet and basalt-covered asphalt. Therefore, in this case, the real and imaginary parts of the synthesized scattering parameters can
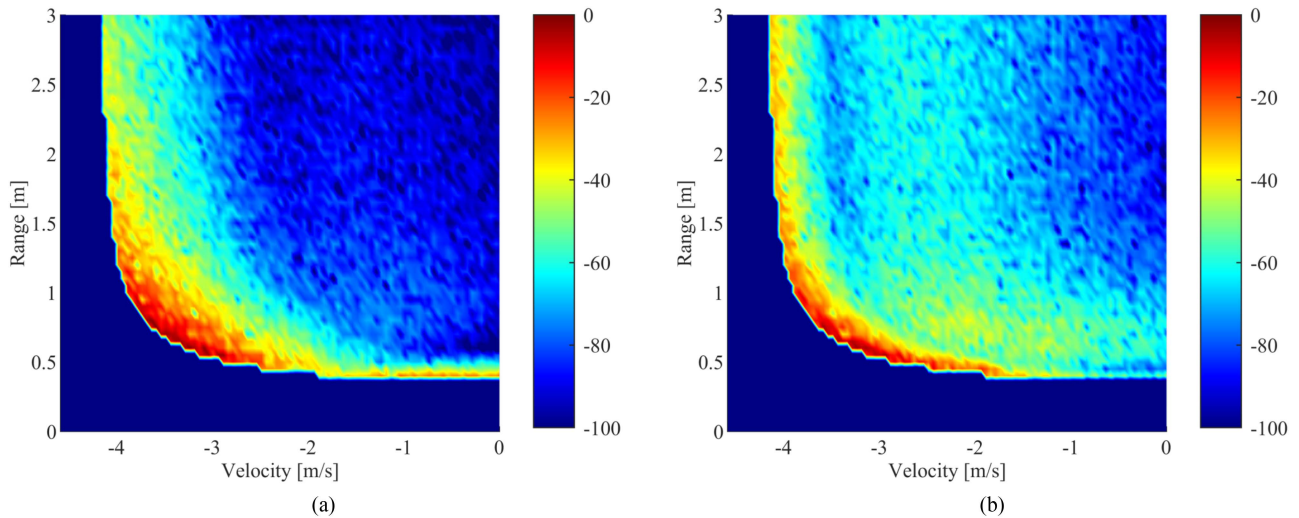
Fig. 6.   Synthesized range–Doppler spectrum of a uniform dry asphalt road surface of a dual-polarized horn antenna with an antenna orientation angle of 60°, moving at a speed of 15 km/h as observed in the (a) VV-polarized channel and (b) HH-polarized channel.
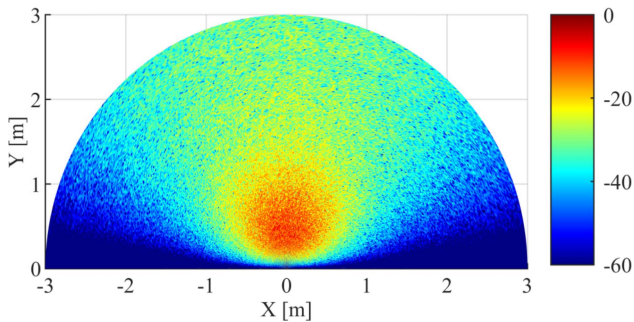

Fig. 7.   Normalized received power from surface scattering elements in the VV-polarized channel simulating dry asphalt, including effects of propagation losses, scattering element surface area, and the gain of a forward-looking cosine-squared antenna at a height of 38 cm.

be modeled as normally distributed random variables with co-variance and mean values as determined during the normalized RCS model derivation procedure. Furthermore, it is important to note that this synthesis method is not limited to normally distributed random variables and, thus, any multivariate distribution can be used to potentially achieve a better fit to the measurement data.

Subsequently, to represent scattering from the road surface, a grid of scattering elements over the road surface is generated. For each scattering element, a full scattering matrix is generated using a multivariate normal distribution with the extracted statistical properties corresponding to the surface type. Next, the contribution of each element to the total received power, including the effects of antenna gain, propagation losses, and surface area of the grid element, is computed following the procedure described in Section III. Fig. 4(a) shows the contributions to the VV-polarized channel from surface elements simulating a dry asphalt surface as seen by a dual-polarized horn antenna, placed at a height of 38 cm with an orientation angle of 60°. In this plot, the effect of the sidelobe of the horn antenna manifests itself as a maximum around the origin. Even

though the sidelobe level of the dual-polarized horn is about −14 dB, the lower gain for the scattering elements near the origin is compensated by the shorter range and corresponding lower propagation losses compared to the scattering elements that lie in the main lobe. As the antenna is placed at a height of 38 cm with an orientation angle of 60°, the point of maximum gain is located at a ground range of about 66 cm directly in front of the antenna. However, the surface scattering elements that provide the strongest contributions to the total backscattered response are centered around 56 cm. This is also caused by the longer range to the scattering element that sees the maximum antenna gain, and thus, higher propagation losses occur, which reduces the total contribution of the elements located around 66 cm compared to those centered around 56 cm directly in front of the antenna.

As described in Section III, a range profile can be found by summing the contributions of each scattering element to their corresponding range bin. The results of this procedure are shown in Fig. 5. In this plot, also a comparison with measurement data from a dry asphalt surface is shown. Excellent agreement can be seen between the simulated and measured range profiles up to a range of 1.5 m. From this range onward, the measurement data of the magnitude of S_{VV} is limited by noise, whereas the simulated range profile shows the expected decrease with the range due to increased propagation losses and decreased antenna gain.

From Fig. 4, also the range–Doppler spectra can be synthesized using the procedure described in Section III. Assuming a platform speed of 15 km/h and adding the surface scattering contributions to their corresponding range–Doppler bins results in the range–Doppler spectra shown in Fig. 6. It can be seen that the range–Doppler signature of the asphalt surface spreads over the Doppler domain due to scattering from the surface area that is not directly in front of the moving platform.

Furthermore, it can be seen that most power is contained in the sector of the range–Doppler plot delimited by the speeds smaller than −2 m/s and ranges closer than 1.5 m to the platform due to the 60° orientation angle of the horn antenna. Also, in the
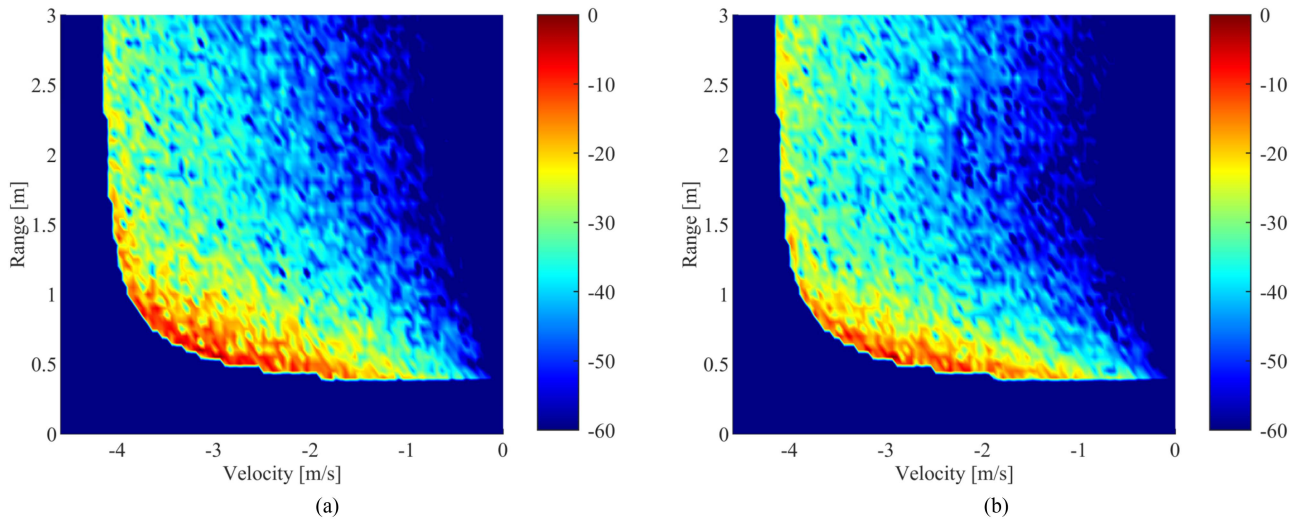
Fig. 8. Synthesized range–Doppler spectrum of a uniform dry asphalt road surface illuminated by a forward-looking antenna with cosine-squared pattern, moving at a speed of 15 km/h as observed in the (a) VV-polarized channel and (b) HH-polarized channel.
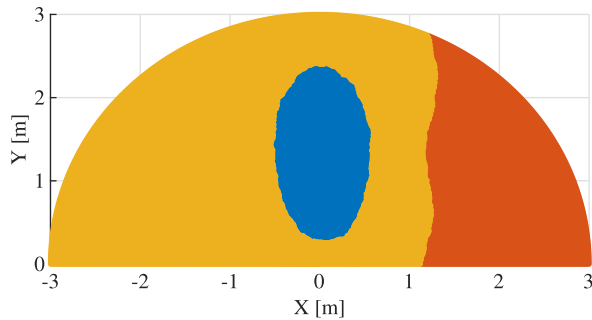

Fig. 9. Road surface conditions definition for a synthesis comprising multiple different surface types. Orange corresponds to dry asphalt while blue and red correspond to wet and basalt-covered asphalt, respectively.
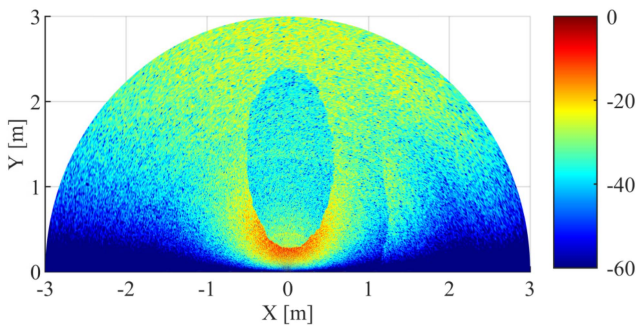

Fig. 10. Normalized received power from surface scattering elements in the HH-polarized channel simulating the scenario from Fig. 9, including effects of propagation losses, scattering element surface area, and the gain of a forward-looking cosine-squared antenna at a height of 38 cm.

VV-polarized channel, a relatively large return in the range–Doppler bins at a range of 0.45 m and at velocities between -1.5 and 0 m/s can be seen. This is due to the sidelobe of the dual-polarized horn antenna, which increases the return from the surface area underneath the antenna.

In the HH-polarized channel, the part of the range–Doppler spectrum bounded by velocities of -3 and -3.5 m/s and a

range larger than 1 m shows relatively less backscattered power compared to the VV-polarized channel while at ranges up to 1 m and velocities higher than -3 m/s, more scattered power is observed. This is also caused by sidelobes of the dual-polarized horn antenna. Namely, in the H-polarized mode of the antenna, the sidelobes are now in the horizontal plane in contrast to the vertical plane as is the case for the V-polarized mode. This results in an effectively wider beam at close range in the HH-polarized channel [see Fig. 4(b)], resulting in a broader spread over the velocity of the backscattered power at these ranges. The nulls between the sidelobes and the main lobe together with the slightly narrower main lobe compared to the V-polarized mode, result in the lower amount of backscattered power in the -3.5 to -3 m/s area of the spectrum.

Instead of a dual-polarized horn antenna with an orientation angle of 60°, also antennas with other radiation patterns can be considered. Fig. 7 shows the contributions of the surface scattering elements to the backscattered power using a forward-looking (90° orientation angle) antenna with a cosine-squared pattern in both elevation and azimuthal planes. Compared to the syntheses with the dual-polarized horn antenna, no sidelobes are present. This leads to a more uniform illumination of the surface, resulting in a more uniform range–Doppler signature, as shown in Fig. 8. As the radiation patterns for both polarized channels are the same in these plots, the effects of the difference between polarizations of the normalized RCS models can be observed as well. Namely, the range–Doppler spectrum of the VV-polarized channel [see Fig. 8(a)] shows a stronger return that is more extended in range than is visible in the HH-polarized range–Doppler spectrum [see Fig. 8(b)]. This is consistent with the normalized RCS model of dry asphalt [see Fig. 2(a)] that shows that the HH-polarized normalized RCS decreases more with the range than the VV-polarized normalized RCS.

Besides surfaces comprising completely of dry asphalt, also surfaces comprising multiple different surface conditions can be simulated. This is done by assigning parts of the surface
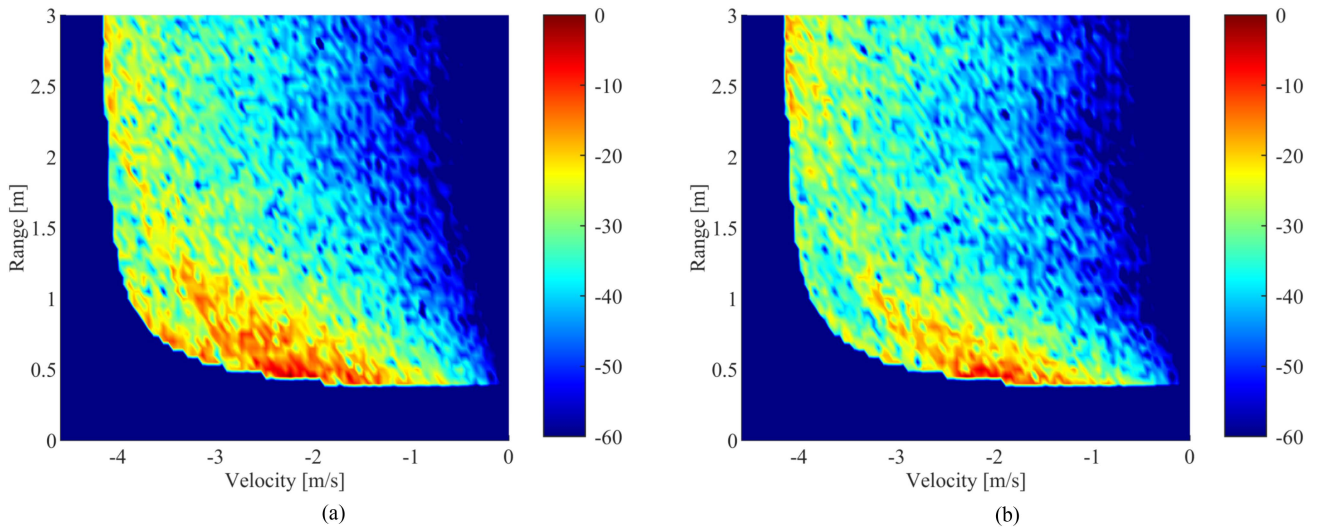
Fig. 11. Synthesized range–Doppler spectrum of the road surface conditions as defined in Fig. 9 using a forward-looking antenna with a cosine-squared pattern, moving at a speed of 15 km/h as observed in the (a) VV-polarized channel and (b) HH-polarized channel.
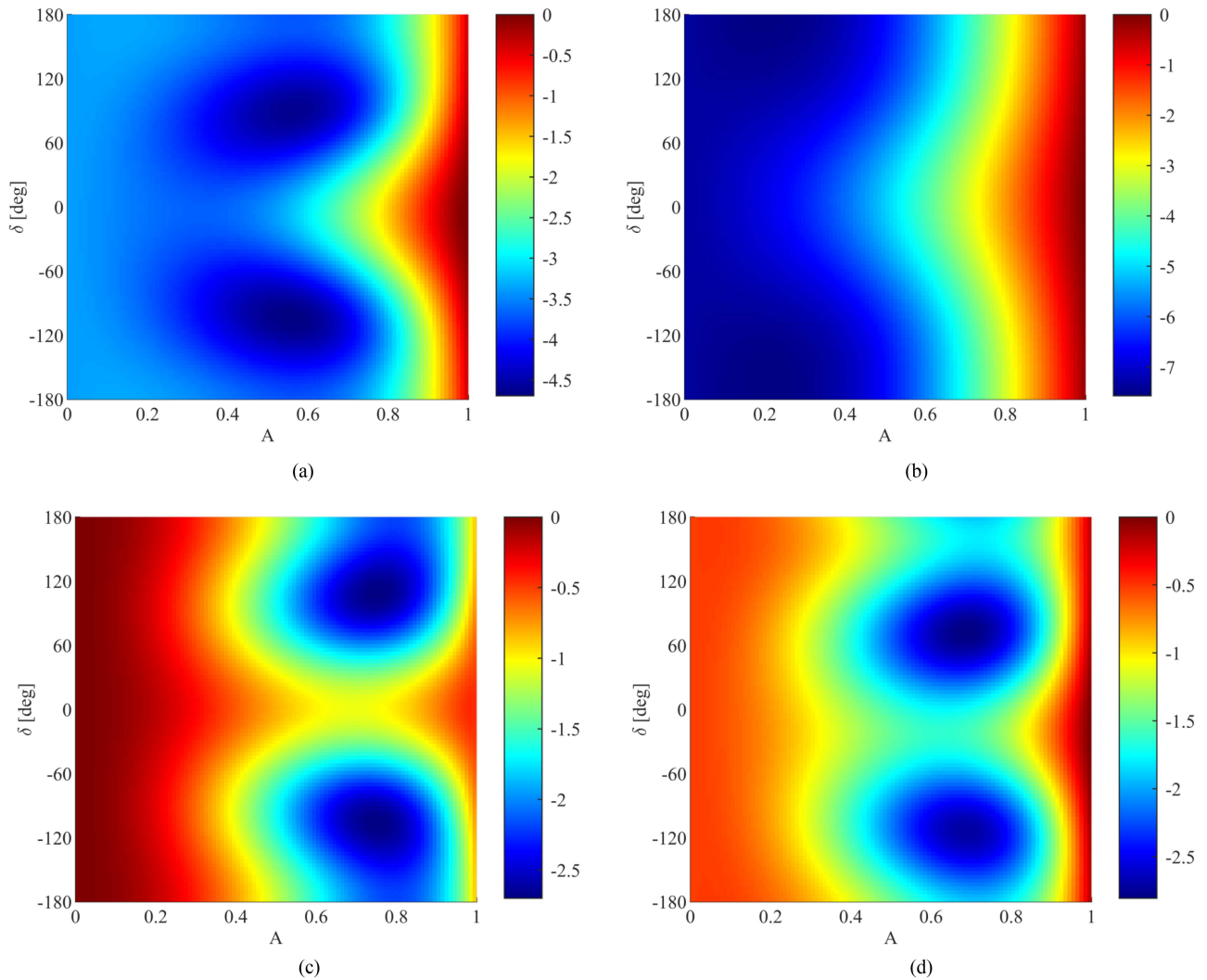

Fig. 12. Normalized returned power in decibels for a single-polarized radar system for the four measured road surface classes at a distance of 68 cm from the antenna located 38 cm above the surface. (a) Dry asphalt. (b) Wet asphalt. (c) Asphalt covered by basalt split ranging in size from 2 to 8 mm. (d) Old asphalt.

scattering elements to different normalized RCS models. An example of such a surface is shown in Fig. 9, which represents a puddle of water in front and gravel to the right-hand side of the vehicle. In this scenario, also a forward-looking antenna with a cosine-squared pattern is used for both polarizations.

The synthesized surface scattering contributions for the HH-polarized channel are shown in Fig. 10. Here, the distinction between the wet and dry asphalt is clearly visible. This is clear from the normalized RCS models, as the normalized RCS of wet asphalt [see Fig. 2(b)] is much lower than that of dry asphalt [see Fig. 2(a)]. The difference between the dry and basalt-covered areas is also visible in Fig. 10. However, the distinction is less clear as the difference between the normalized RCS of basalt-covered asphalt [see Fig. 2(c)] and dry asphalt is smaller than the difference with wet asphalt.

Also, range–Doppler spectra can be generated from Fig. 10 and its VV-polarized counterpart. This is shown in Fig. 11. Compared to the range–Doppler spectra of a uniform dry asphalt surface (see Fig. 8), it can be seen that the power in the -4 to -3 m/s sector is reduced due to the decreased backscattering caused by the puddle of water. Also, in the HH-polarized channel, a diagonal line starting at a velocity of -1 m/s and a range of 1.4 m is visible. This line corresponds to the gravel on the side of the road, which is about this distance away from the radar antenna. Note that it is easier to observe this line in the HH-polarized channel as the contrast between the gravel and dry asphalt is larger due to the larger difference in normalized RCS in this channel as can be seen from Fig. 2(a) and (c).

Finally, it should be noted that in this section, the presented synthesis results were computed up to a distance of 3 m as the normalized RCS is the largest and shows the most variation in this area. This distance is likely still enough for, e.g., automatic antilock braking system adjustments given the processing capabilities of modern automotive onboard computers even when the vehicle's velocity is significant. However, the proposed synthesis method can be made arbitrarily large and is limited only by the accuracy of the statistical normalized RCS models at shallow angles of incidence that correspond to these larger ranges.

C. Optimal Polarization Selection

The models of the normalized RCS of the road surface types can also be used to determine the optimal sensing wave polarization for single-polarized radar and other polarimetric applications such as filters to increase or suppress scattering from road surfaces. By factorizing the antenna polarization vector in two quantities, the optimal polarization for minimizing or maximizing the received power from a target of interest can be determined numerically, as described in Section IV.

As an example, this procedure is performed on the four different measured road surface types. The results for the normalized RCS models at a distance of 68 cm, the distance at which the surface scattering contributions are highest, are shown in Fig. 12. These figures show the normalized received power as the function of sensing wave polarization. It can be seen that in the case of dry, wet, and old asphalt, maximum received power is achieved for a value of A of 1, which corresponds to vertical polarization.

In the case of basalt-covered asphalt, horizontal polarization ($A = 0$) would result in maximum received power. However, as can be seen from Fig. 12(c), using vertical polarization results for basalt-covered asphalt in a loss of less than 1 dB compared to a horizontally polarized sensing wave. This observation is backed up by the normalized RCS models as shown in Fig. 2(c), as the normalized VV-polarized RCS is within 1 dB of the normalized HH-polarized RCS. Therefore, it can be concluded that for a single-polarized radar system, a vertically polarized sensing wave is optimal when the goal is to maximize the backscattered return from the measured road surface types.

However, the situation for suppressing returns from the road surface is less obvious as all four measured road surface classes have their minima located at different polarizations. In the case of wet asphalt, minimal return is achieved at linear polarization that is slightly offset from horizontal polarization ($A \approx 0.2$, $\delta \approx \pm 180°$) while for the other three classes, elliptical polarizations should be used. In the case of dry asphalt, a polarization with $A \approx 0.55$ and $\delta \approx \pm 100°$ would yield best results, whereas, for basalt-covered asphalt, a polarization with $A \approx 0.75$ and $\delta \approx \pm 100°$ would. In the case of old asphalt, a polarization with $A \approx 0.7$ and $\delta \approx 70°$ would result in minimal returned power.

Since there is no polarization that achieves minimal received power for all road surface condition classes, a designer of a single-polarized radar system must perform a tradeoff to achieve optimal performance regarding antenna polarization. For example, the designer must consider the relative frequency with which the road surface conditions occur. Namely, if the wet and basalt-covered road surface conditions are expected to show up very rarely, it would be beneficial to select the polarization that achieves minimal received power for dry asphalt. Another consideration that may play a role is the absolute amount of power received from a road surface type, e.g., power backscattered from wet asphalt could already be negligible compared to that from the targets-of-interest, and thus, the wet asphalt could be left out of the analysis.

Thus, to reach optimal performance regarding the signal-to-clutter ratio, in practice, a designer has to formulate a score function that should, for example, contain weighting factors based on the relative frequency of appearance of the to-be-suppressed clutter type, as well as the magnitude of the RCS of said clutter. Also, the score function should contain weights for the RCS models of targets-of-interest based on the same factors as previously mentioned for clutter to increase the received power from the desired targets as much as possible to eventually maximize the signal-to-clutter ratio.

VII. Conclusion

In this article, a novel method of deriving the statistical properties of surface backscattering from range profile measurements is proposed. The method is based on modeling the surface as a collection of uncorrelated scattering elements, with all elements having a normalized scattering matrix that is characterized by a multivariate distribution. Assuming the surface-under-test is isotropic and that all surface scattering elements within one range bin experience the same angle of incidence, it is shown that

the mean value and covariance can be computed from measured range profile data.

This method is then applied to measurement data collected with a VNA equipped with a dual-polarized horn antenna in the frequency band ranging from 75 to 85 GHz. It is shown that the statistical properties of two different types of asphalt as well as three different road surface conditions could be determined successfully, thus demonstrating the general applicability of the method. Specifically, relatively new unused and heavily used old asphalt were considered where the new asphalt type was measured in three different conditions, which were dry, wet, and covered with basalt gravel. It is shown that gravel-covered asphalt and old asphalt behave as an electromagnetically rough surface as both magnitudes of copolarized RCSs are on the same level and show a decay as the function of incident angle corresponding to a cosine, leading to the conclusion that these surface classes resemble Lambertian scattering behavior. For the dry and wet asphalt surface types, the copolarized RCSs show an increasing difference between the vertically and horizontally polarized RCS with an increase in the incident angle. In the case of dry asphalt, this difference increases from less than 1 dB to over 4 dB in favor of the vertically polarized RCS. In the case of wet asphalt, the RCS was found to be over 10 dB lower than that of dry asphalt. As with the RCS of dry asphalt, the HH-polarized RCS decreases with incident angle quicker than the VV-polarized RCS. Furthermore, it can be seen that the contribution of multiple scattering events to the total received backscattered power is relatively marginal for all four road surface classes as the cross-polarized RCSs are significantly lower than the co-polarized ones.

Furthermore, two applications of the derived statistical normalized RCS models are proposed. First, a novel procedure to synthesize surface clutter in range profiles, range–angle plots, and range–Doppler spectra is proposed. This procedure is subsequently applied to simulate range profiles and range–Doppler spectra of a dry asphalt surface, and excellent agreement with measured range profiles is shown. The procedure is also demonstrated to be able to simulate surface scattering from a surface consisting of multiple different road surface conditions. It is shown that, for example, a puddle of water in front of the radar platform and gravel to the side of the platform, respectively, de-emphasize and emphasize corresponding areas in the range–Doppler spectrum.

Second, a novel method for determining the optimal sensing wave polarization for a single-polarized radar system based on (statistical) RCS models is presented. This procedure utilizes a factorization of the antenna polarization vector in two different parameters, namely A and δ. Since these parameters are, respectively, bounded by 0 and 1 and $-180°$ and $+180°$, the maxima and minima of the received power can be found numerically. It is shown that the optimal sensing wave polarization depends on the intended application of the radar system and that the proposed method can be used to find this optimum. Using the proposed procedure and the normalized RCS models of the four measured road surface types, it is determined that a V-polarized sensing wave is optimal to maximize the return from the road surface, which is beneficial when the automotive radar system is intended for, e.g., road surface conditions classification. For

different applications, it is demonstrated that to find the optimal polarization for a single-polarized radar system to achieve optimal signal-to-clutter ratio, a score function that includes among others weighting factors for each considered target class based on the relative frequency of appearance and the magnitude of the RCS of such a target has to be defined. By subsequently using this score function in conjunction with the proposed method, the optimal polarization for the radar application corresponding to that score function can be determined.

References

[1] P. Hindle, "Comprehensive survey of 77, 79 GHz automotive radar companies sensors and ICs," *Microw. J.*, Mar. 2020. [Online]. Available: https://www.microwavejournal.com/articles/33705-comprehensive-survey-of-77-79-ghz-automotive-radar-companies-sensors-and-ics

[2] G. Hakobyan and B. Yang, "High-performance automotive radar: A review of signal processing algorithms and modulation schemes," *IEEE Signal Process. Mag.*, vol. 36, no. 5, pp. 32–44, Sep. 2019.

[3] S. Trummer, G. F. Hamberger, R. Koerber, U. Siart, and T. F. Eibert, "Performance analysis of 79 GHz polarimetric radar sensors for autonomous driving," in *Proc. Eur. Radar Conf.*, 2017, pp. 41–44.

[4] H. Iqbal, F. Bögelsack, and C. Waldschmidt, "Polarimetric RCS analysis of traffic objects," in *Proc. Eur. Radar Conf.*, 2017, pp. 49–52.

[5] V. Vassilev, "Road surface recognition at mm-wavelengths using a polarimetric radar," *IEEE Trans. Intell. Transp. Syst.*, vol. 23, no. 7, pp. 6985–6990, Jul. 2022.

[6] S. M. Sabery, A. Bystrov, P. Gardner, A. Stroescu, and M. Gashinova, "Road surface classification based on radar imaging using convolutional neural network," *IEEE Sensors J.*, vol. 21, no. 17, pp. 18725–18732, Sep. 2021.

[7] C. Schüßler, M. Hoffmann, J. Bräunig, I. Ullmann, R. Ebelt, and M. Vossiek, "A realistic radar ray tracing simulator for large MIMO-arrays in automotive environments," *IEEE J. Microw.*, vol. 1, no. 4, pp. 962–974, Oct. 2021.

[8] D. He et al., "Channel measurement and ray-tracing simulation for 77 GHz automotive radar," *IEEE Trans. Intell. Transp. Syst.*, vol. 24, no. 7, pp. 7746–7756, Jul. 2023.

[9] M. M. Zaky and K. Sarabandi, "Fully coherent electromagnetic scattering computation for snowpacks based on statistical S-matrix approach," *IEEE Trans. Geosci. Remote Sens.*, vol. 59, no. 8, pp. 6336–6345, Aug. 2021.

[10] G. Di Martino, A. Iodice, D. Poreh, and D. Riccio, "Pol-SARAS: A fully polarimetric SAR raw signal simulator for extended soil surfaces," *IEEE Trans. Geosci. Remote Sens.*, vol. 56, no. 4, pp. 2233–2247, Apr. 2018.

[11] M. M. Tajdini, B. Gonzalez-Valdes, J. A. Martinez-Lorenzo, A. W. Morgenthaler, and C. M. Rappaport, "Real-time modeling of forward-looking synthetic aperture ground penetrating radar scattering from rough terrain," *IEEE Trans. Geosci. Remote Sens.*, vol. 57, no. 5, pp. 2754–2765, May 2019.

[12] V. Volosyuk, V. Pavlikov, M. Nechyporuk, S. Zhyla, N. Ruzhentsev, and V. Kosharskyi, "Optimal algorithms synthesis for polarization selection of useful signals on the background of passive interference in synthetic aperture radars," in *Proc. IEEE Int. Conf. Problems Infocommunications. Sci. Technol.*, 2020, pp. 452–456.

[13] L. Iannini, D. Comite, N. Pierdicca, and P. Lopez-Dekker, "Rough-surface polarimetry in companion SAR missions," *IEEE Trans. Geosci. Remote Sens.*, vol. 60, pp. 1–15, Apr. 2022.

[14] P. Asuzu and C. Thompson, "Road condition identification from millimeter-wave radar backscatter measurements," in *Proc. IEEE Radar Conf.*, 2018, pp. 0012–0016.

[15] K. Sarabandi, E. Li, and A. Nashashibi, "Modeling and measurements of scattering from road surfaces at millimeter-wave frequencies," *IEEE Trans. Antennas Propag.*, vol. 45, no. 11, pp. 1679–1688, Nov. 1997.

[16] M. Giallorenzo, X. Cai, A. Nashashibi, and K. Sarabandi, "Radar backscatter measurements of road surfaces at 77 GHz," in *Proc. IEEE Int. Symp. Antennas Propag. USNC/URSI Nat. Radio Sci. Meeting*, 2018, pp. 2421–2422.

[17] X. Meng, P. Li, Y. Hu, F. Song, and J. Ma, "Theoretical study on recognition of icy road surface condition by low-terahertz frequencies," *IEEE Trans. Geosci. Remote Sens.*, vol. 60, pp. 1–9, Jun. 2022.

[18] T. J. Douglas, A. Y. Nashashibi, M. Kashanianfard, and K. Sarabandi, "Polarimetric backscatter measurements of road surfaces at J-band frequencies for standoff road condition assessment," in *Proc. IEEE USNC-URSI Radio Sci. Meeting (Joint With AP-S Symp.)*, 2021, pp. 35–36.

[19] V. V. Viikari, T. Varpula, and M. Kantanen, "Road-condition recognition using 24-GHz automotive radar," *IEEE Trans. Intell. Transp. Syst.*, vol. 10, no. 4, pp. 639–648, Dec. 2009.

[20] W. Bouwmeester, F. Fioranelli, and A. Yarovoy, "Statistical polarimetric RCS model of an asphalt road surface for mm-Wave automotive radar," in *Proc. 20th Eur. Radar Conf.*, 2023, pp. 18–21.

[21] W. Bouwmeester, F. Fioranelli, and A. Yarovoy, "Dynamic road surface signatures in automotive scenarios," in *Proc. 18th Eur. Radar Conf.*, 2022, pp. 285–288.

[22] C. A. Balanis, *Antenna Theory: Analysis and Design*, 4th ed. Hoboken, NJ, USA: Wiley, 2016.

[23] J.-S. Lee and E. Pottier, *Polarimetric Radar Imaging: From Basics to Applications*. Boca Raton, FL, USA: CRC Press, Jan. 2017.

[24] W. Bouwmeester, F. Fioranelli, and A. Yarovoy, "Road surface conditions identification via H α A decomposition and its application to mm-Wave automotive radar," *IEEE Trans. Radar Syst.*, vol. 1, pp. 132–145, Jun. 2023.

[25] G. P. Kulemin, *Millimeter-Wave Radar Targets and Clutter (Ser. Artech House Radar Library)*. Boston, MA, USA: Artech House, 2003.

Wietse Bouwmeester (Graduate Student Member, IEEE) received the B.Sc. degree in electrical engineering from the Delft University of Technology, Delft, The Netherlands, in 2016, the M.Sc. degree in electrical engineering from the Delft University of Technology in 2020, with a focus on telecommunications and sensing systems (*cum laude*), focusing on the design of a conformal phased array antenna commissioned by ASTRON, the Dutch institute for radio astronomy.

In 2020, he joined the Microwave Sensing, Signals and Systems group, TU Delft, as a Ph.D. Candidate, and is currently working there on polarimetric approaches to classify road surfaces and other targets with mm-Wave radar for automotive applications.

Francesco Fioranelli (Senior Member, IEEE) received the Laurea (B.Eng., *cum laude*) and Laurea Specialistica (M.Eng., *cum laude*) degrees in telecommunication engineering from Università Politecnica delle Marche, Ancona, Italy, in 2007 and 2010, respectively, and the Ph.D. degree in electronic engineering from Durham University, Durham, U.K., in 2014.

He is currently an Associate Professor with TU Delft, Delft, The Netherlands, and was an Assistant Professor with the University of Glasgow from 2016 to 2019 and a Research Associate with University College London from 2014 to 2016. He has authored more than 160 publications between book chapters, journal, and conference papers and edited the books *Micro-Doppler Radar and Its Applications* and *Radar Countermeasures for Unmanned Aerial Vehicles* (IET-Scitech) in 2020. His research interests include the development of radar systems and automatic classification for human signatures analysis in healthcare and security, drones and UAVs detection and classification, automotive radar, wind farm, and sea clutter.

Dr. Fioranelli is a recipient of four best paper awards.

Alexander G. Yarovoy (Fellow, IEEE) received the Diploma (with Hons.) degree in radiophysics and electronics from Kharkov State University, Kharkiv, Ukraine, in 1984, and the Candidate of Physics and Mathematical Sciences and the Doctor of Physics and Mathematical Sciences degrees in radiophysics in 1987 and 1994, respectively.

In 1987, he joined the Department of Radiophysics, Kharkov State University, as a Researcher, and became a Full Professor there in 1997. From September 1994 to 1996, he was with the Technical University of Ilmenau, Germany, as a Visiting Researcher. Since 1999, he has been with the Delft University of Technology, Delft, The Netherlands. Since 2009, he has been leading the Microwave Sensing, Systems and Signals group as a Chair. He has authored and coauthored more than 500 scientific or technical papers, six patents, and 14 book chapters. His main research interests include high-resolution radar, microwave imaging, and applied electromagnetics (in particular, UWB antennas).

Dr. Yarovoy is the recipient of the European Microwave Week Radar Award for the paper that best advances the state of the art in radar technology in 2001 (together with L.P. Ligthart and P. van Genderen) and in 2012 (together with T. Savelyev). In 2010, together with D. Caratelli, he got the best paper award of the Applied Computational Electromagnetic Society (ACES). He was the General TPC Chair of the 2020 European Microwave Week, the Chair and TPC Chair of the 5th European Radar Conference, and the Secretary of the 1st European Radar Conference. He was also the Cochair and the TPC Chair of the Xth International Conference on GPR. He is currently an Associate Editor for IEEE TRANSACTION ON RADAR SYSTEMS. From 2011 to 2018, he was an Associate Editor for the *International Journal of Microwave and Wireless Technologies*. From 2008 to 2017, He was the Director of the European Microwave Association.